ARCHIVES OF MECHANICS
Arch. Mech. **77** (1), 67–85, 2025, DOI: 10.24423/aom.4629

Development of a computational framework for low-Reynolds number propeller aeroacoustics

O. SZULC, T. SURESH, P. FLASZYŃSKI

Institute of Fluid-Flow Machinery, Polish Academy of Sciences, Fiszera 14, 80-231 Gdansk, Poland, e-mail: oskar.szulc@imp.gda.pl

The paper focuses on the development and validation of a new computational framework designed for the prediction of tonal and broadband noise radiation of propellers of unmanned aerial vehicles (UAVs) operating in the low-Reynolds number regime. The depicted workflow is hybrid, consisting of in-house, academic, and commercial software components intended for automatic pre-processing (block-structured grid generation), efficient flow solution (computational fluid dynamics, CFD), and acoustic post-processing (computational aeroacoustics, CAA). The delayed detached-eddy simulation (DDES) approach constitutes the basis for estimation of mean blade loading and surface pressure fluctuations due to the existence of massive flow separation that are fed as input to an in-house acoustic solver based on Ffowcs Williams and Hawkings (FW–H) linear acoustic analogy (Farassat's formulation 1A). The initial phase of validation of the acoustic tool is conducted for elementary rotating and oscillating point sources of mass and momentum (forces) using available analytical solutions for reference. Later, a two-bladed model propeller from the Delft University of Technology (TUD) is analyzed with FLOWer (compressible CFD solver from DLR), relying on RANS or DDES approaches and equipped with either 1-equation strain adaptive linear Spalart–Allmaras or 2-equation shear-stress transport k–ω turbulence closures. The equations are solved using both classical second-order and modern fourth-order accurate numerical schemes. For a selected rotational speed of 5000 RPM (tip Mach number of 0.23 and tip Reynolds number of $50 \cdot 10^3$) and the range of the advance ratio J of the axial flight, the predicted propeller aerodynamic performance is confronted with the measurements of TUD. Lastly, for exemplary $J = 0$ (hover conditions, tripped boundary layer), the resolved pressure fluctuations (URANS/k–ω SST and DDES/k–ω SST) are directly used as input for acoustic analysis of tonal (harmonic) and broadband noise at an in-plane observer location and the resultant propeller sound pressure level signature is compared with the measured spectrum confirming the applicability of the developed framework for such computationally demanding cases of flow-induced noise.

Key words: UAV propeller, computational fluid dynamics (CFD), computational aeroacoustics (CAA), FLOWer, RANS, delayed detached-eddy simulation (DDES), Ffowcs Williams and Hawkings (FW–H) analogy, Farassat's formulation 1A (impermeable surface).

Notation

c	chord length, m,
c_0	reference (ambient) speed of sound, $\mathrm{m} \cdot \mathrm{s}^{-1}$,
c_q	rotor shaft torque coefficient,
c_t	rotor thrust coefficient,
D	rotor diameter, m,
f	frequency, Hz,
f_osc	frequency of oscillation, Hz,
f_rot	frequency of rotation, Hz,
F_t	rotor thrust force, N,
$F(\tau)$	force vector (F) magnitude, N,
M_q	rotor shaft torque, $\mathrm{N} \cdot \mathrm{m}$,
J	advance ratio,
M_i	Mach number vector (M) components,
M_r	Mach number in the radiation direction,
M_T	tip Mach number,
n_i	normal vector (n) components,
N	sample count,
OASPL	overall sound pressure level, dB,
p	surface pressure, Pa,
p_0	reference (ambient) pressure, Pa,
p'	total acoustic pressure, Pa,
p'_L	acoustic pressure due to aerodynamic forces (loading noise), Pa,
p'_ref	threshold of human hearing, Pa,
p'_rms	root mean square of acoustic pressure, Pa,
p'_T	acoustic pressure due to mass displacement (thickness noise), Pa,
r	distance between the source and the observer, m,
r_i	radiation vector (r) components, m,
$\hat{r}_i$	unit radiation vector ($\hat{\mathrm{r}}$) components,
R	rotor radius, m,
Re_T	tip Reynolds number,
S	acoustic source surface,
SPL	sound pressure level, dB,
t	observer (reception) time, s,
T_0	reference (ambient) temperature, K,
T_rot	period of rotation, s,
u_i	velocity vector (u) components, $\mathrm{m} \cdot \mathrm{s}^{-1}$,
u_n	normal velocity component, $\mathrm{m} \cdot \mathrm{s}^{-1}$,
U_T	tip velocity, $\mathrm{m} \cdot \mathrm{s}^{-1}$,
U_0	free-stream axial flow velocity, $\mathrm{m} \cdot \mathrm{s}^{-1}$,
x_i	observer space coordinates (x), m,
y_i	source space coordinates (y), m,
y^+	non-dimensional distance to the surface.

Greek letters

δ	Dirac delta function,
Δp	surface gauge pressure $p - p_0$, Pa,
Δt	time-step, s,
$\Delta \tau$	acoustic time-step, s,

η_i body-fixed space coordinates (η), m,
η_{prop} rotor propulsive efficiency,
θ twist angle, rad,
θ_r angle between the surface normal (n) and the radiation (r) vectors, rad,
ρ_0 reference (ambient) density, $\text{kg} \cdot \text{m}^{-3}$,
τ retarded (emission) time, s.

1. Introduction

TWO MAJOR CHALLENGES ARISE IN THE NUMERICAL ANALYSIS of low-Reynolds number (10^4–10^5) propellers utilized in Unmanned Aerial Vehicles (UAVs). Firstly, significant broadband noise emissions highlight the necessity for scale-resolving simulations that can take into account laminar-turbulent transition and accurately model separation bubbles in both laminar and turbulent flow. Secondly, there is a need for high-quality experimental data that integrates force, flow, and noise measurements under controlled conditions [1]. For such configurations, scale-resolved methods such as the lattice Boltzmann method (LBM)/very large-eddy simulation (VLES) [2], detached-eddy simulation (DES) [3], or specific variants of hybrid RANS/large-eddy simulation (LES) methods are typically employed for aeroacoustic applications. Tonal noise emission is usually attributed to thickness (mass displacement effect) and steady loading (mean aerodynamic forces) sources [4]. However, the broadband noise radiation is linked to flow-induced surface pressure fluctuations, which may arise from various sources, e.g., the scattering of the turbulent eddies in the boundary layer by the trailing edge (trailing edge noise, TEN), by the inflow turbulence impacting the leading edge (turbulence ingestion noise, TIN), by the blade-vortex (BVI), or blade-wake (BWI) interactions taking place at low advance ratios [5]. Nevertheless, for small-scale propellers, the primary source of surface pressure fluctuations is linked to unsteady laminar separation bubbles (including laminar shear-layer instability) and the detachment of turbulent boundary layers, which contribute to separation noise (SN) [6, 7]. Among the various methods for predicting propeller tonal and broadband noise, the hybrid CFD/CAA approach is of primary interest. In particular, combining high-fidelity near-field CFD with the Ffowcs Williams and Hawkings (FW–H) acoustic analogy, using either on-surface or porous variants, for source generation and propagation (Farassat's formulation 1A) proves advantageous [2, 3, 5, 8, 9]. In this approach, far-field noise is determined based on the body geometry, kinematics, and surface pressure distribution (steady or unsteady) obtained from CFD.

This paper is organized as follows. Section 2 provides a brief overview of the implemented general FW–H acoustic analogy, derived for arbitrarily moving bodies (Farassat's formulation 1A), along with an elementary analytical solution for a rotating point source of momentum. Section 3 outlines the validation

process of the FW–H solver for an oscillating and rotating point force scenario. Section 4 is entirely devoted to the application of the FW–H code in the aerodynamic and aeroacoustic analysis of a low-Reynolds number propeller. It includes a detailed specification of the computational model designed for predicting the propeller flow-field, validated against wind tunnel measurements of rotor aerodynamic loading. The resulting steady loading and unsteady surface pressure fluctuations due to separation serve as input data for the subsequent FW–H analysis of thickness, steady and unsteady loading noise sources, enabling final validation of the computed sound pressure level (SPL) spectra against available experimental data. The conclusions of the paper are briefly summarized in Section 5.

2. Theoretical basis

2.1. Ffowcs Williams and Hawkings inhomogenous wave equation

The Ffowcs Williams and Hawkings (FW–H) inhomogeneous linear wave equation is a key equation in aeroacoustics, utilized to model noise produced by moving surfaces in a fluid like air [10]:

$$\frac{\partial^2 p'}{\partial t^2} - c_0^2 \nabla^2 p' = \frac{\partial}{\partial t}[\rho_0 u_n \delta(S)] - \frac{\partial}{\partial x_i}[\Delta p\, n_i \delta(S)], \tag{2.1}$$

where p' is the acoustic pressure, t is the observer (reception) time, x_i are the spatial coordinates (Cartesian), n_i are the local normal vector n components, $\frac{\partial^2}{\partial t^2}$ and ∇^2 are the temporal and the Laplacian operators, c_0 and ρ_0 are the speed of sound and the ambient density (both assumed constant). Next, $u_n = \mathrm{u} \cdot \mathrm{n}$ and Δp signify the normal velocity of the surface (u – panel velocity vector) and the surface gauge pressure ($\Delta p = p - p_0$, p_0 – ambient pressure), determining the strengths of the monopole and dipole sources (quadrupole sources are neglected), respectively. Furthermore, $\delta(S)$ represents the Dirac delta function, which ensures that the source terms are only active at the surface of the moving body, where $S(\mathrm{x}, t) = 0$. This equation can be specialized or altered depending on the assumptions about the flow and the body motion. Farassat proposed various formulations, including formulation 1A, designed to simplify the computation of these terms under particular flow conditions and presumptions, allowing for a more efficient computational implementation or a more tractable evaluation of the source terms [11].

2.2. Farrasat's general solution (formulation 1A) to FW–H equation

The analytical (integral) solution to Eq. (2.1), suitable for propeller or helicopter rotor blades in arbitrary subsonic motion (formulation 1A), was proposed by Farassat (2007) for an impermeable (non-porous) acoustic source sur-

face S [11]. It is expressed as the sum of thickness (mass displacement) p'_{T} and loading (aerodynamic forces) p'_{L} contributions, i.e. $p'(\mathrm{x},t) = p'_{\mathrm{T}}(\mathrm{x},t) + p'_{\mathrm{L}}(\mathrm{x},t)$ where:

$$4\pi\, p'_{\mathrm{T}}(\mathrm{x},t) = \int_S \left[\frac{\rho_0\, \dot{u}_n}{r(1-M_r)^2} + \frac{\rho_0\, u_n\, \hat{r}_i\, \dot{M}_i}{r(1-M_r)^3} + \frac{\rho_0\, c_0\, u_n(M_r - M^2)}{r^2(1-M_r)^3}\right]_{\mathrm{ret}} dS, \tag{2.2}$$

$$4\pi\, p'_{\mathrm{L}}(\mathrm{x},t) = \int_S \left[\frac{\dot{p}\, \cos\theta_r}{c_0\, r(1-M_r)^2} + \frac{\hat{r}_i\, \dot{M}_i\, \Delta p\, \cos\theta_r}{c_0\, r(1-M_r)^3} + \frac{\Delta p(\cos\theta_r - M_i\, n_i)}{r^2(1-M_r)^2} + \frac{(M_r - M^2)\Delta p\, \cos\theta_r}{r^2(1-M_r)^3}\right]_{\mathrm{ret}} dS. \tag{2.3}$$

In this context, (x,t) and (y,τ) denote the observer and source space-time variables within the non-moving (inertial) reference frame, whereas the $\eta = \eta(\mathrm{y},\tau)$ frame remains fixed with respect to the body surface. Hence, the radiation vector $\mathrm{r} = \mathrm{x} - \mathrm{y}$, the distance between the source and the observer $r = |\mathrm{x} - \mathrm{y}|$, the unit radiation vector $\hat{\mathrm{r}} = (\mathrm{x} - \mathrm{y})/r$, the Mach number vector $\mathrm{M} = \mathrm{u}/c_0$, the Mach number in the radiation direction $M_r = \hat{\mathrm{r}} \cdot \mathrm{M}$, cosine of the angle between the surface normal and the unit radiation vectors $\cos\theta_r = \mathrm{n} \cdot \hat{\mathrm{r}}$, and all remaining variables are evaluated in the η-frame at the retarded (emission) time $\tau = t - r/c_0$, indicated by the subscript "ret". The dot notation signifies differentiation with respect to source time, i.e. $\dot{u}_n = \frac{\partial u_n}{\partial \tau} = \frac{\partial}{\partial \tau}(\mathrm{u} \cdot \mathrm{n})$, $\dot{M}_i = \frac{\partial M_i}{\partial \tau} = \frac{1}{c_0}\frac{\partial u_i}{\partial \tau}$, and $\dot{p} = \frac{\partial p}{\partial \tau}$. For each component of Eq. (2.2) and Eq. (2.3), the inverse distance dependence may be identified, with the following distinction into near- and far-field terms based on the $1/r^2$ or $1/r$ proportionality factors, respectively.

2.3. Elementary solution to FW–H (moving point force)

The solution to Eq. (2.1) for a point force $\mathrm{F}(\tau)$ in arbitrary motion is analytically formulated as [12]:

$$4\pi\, p'_{\mathrm{L}}(\mathrm{x},t) = \left[\frac{\mathrm{r} \cdot \dot{\mathrm{F}} - c_0\, \mathrm{M} \cdot \mathrm{F}}{c_0\, r^2(1-M_r)^2} + (\mathrm{r} \cdot \mathrm{F})\frac{\mathrm{r} \cdot \dot{\mathrm{M}} + c_0(1-M^2)}{c_0\, r^3(1-M_r)^3}\right]_{\mathrm{ret}} \tag{2.4}$$

with all parameters computed at the retarded (emission) time $\tau = t - r/c_0$ (subscript "ret"). The dot over the force vector F signifies the differentiation with respect to the source time τ, i.e. $\dot{\mathrm{F}} = \frac{\partial \mathrm{F}}{\partial \tau}$.

3. FW–H solver validation (moving point force)

3.1. In-house FW–H acoustic solver (Tecplot 360 EX)

An FW–H acoustic solver was developed in-house using Tecplot 360 EX (Tecplot Inc.) macro command language directives [13]. It is based on the general so-

lution to FW–H equation (2.1) proposed by Farassat as formulation 1A and represented by Eq. (2.2) and Eq. (2.3). A block-structured surface mesh and CFD flow data can be directly implemented to specify both the source geometry (rotor blade shape) and the acting forces (surface pressure distribution). Each grid cell is considered an individual acoustic panel, tracked in space-time, and acts as a distinct source of acoustic perturbations. As a first step, the integrands of Eq. (2.2) and Eq. (2.3) are evaluated at the retarded time τ for each acoustic panel. Next, the integrands are summed across all acoustic panels (integration) based on the reception time t at the observer's position, using linear interpolation. This implies that the final shape of the signal depends not only on the local history of each acoustic panel but also on their spatial distribution, which affects the arrival time, leading to constructive or destructive interference. Thickness noise analysis requires solely the surface mesh and blade kinematics while loading noise prediction additionally necessitates the steady or unsteady surface pressure distribution that is usually supplied from a preceding CFD analysis.

The thickness and steady loading noise prediction capabilities of the FW–H solver have already been thoroughly validated in [13] for elementary rotating point sources of mass and momentum (force) with subsequent application to a hovering helicopter rotor case (low-frequency in-plane harmonic noise, LF-IPH). However, for low-Reynolds number UAV propellers, operating mostly under separated flow conditions, induced surface pressure fluctuations significantly contribute to broadband noise emission. Consequently, the FW–H solver has been extended to account for the unsteady forces acting on the rotor blades. As detailed below, a relevant elementary case involving a rotating and oscillating point source of momentum (force) has been selected to validate this new functionality.

3.2. Specification of the elementary aeroacoustic problem

To thoroughly validate the implementation, an exemplary case of a rotating and oscillating point source of momentum (force) is selected as the origin of loading noise. The considered unsteady force vector $\mathrm{F}(\tau)$ is parallel to the rotor plane while rotating around the azimuth with 5000 RPM and at the radius of $R = 0.15$ m, emulating the movement of the sectional drag force of the tip section of the propeller blade investigated in Section 4 (see Fig. 1). The observer is located in the rotor plane, 1.2 m from the axis of rotation (equivalent to $8R$). An arbitrary unsteady force magnitude $F(\tau) = 0.02 + 0.002\sin(2\pi\, f_{\mathrm{osc}}\, \tau)$, characterized by a constant mean value (representing the average aerodynamic force) and overlaying sinusoidal oscillations (often attributed to the presence of boundary layer separation), is selected for analysis. To ensure clear separation of steady and unsteady loading noise contributions, the amplitude of oscillations (0.002 N) represents 10% of the average (0.02 N). Moreover, the frequency of

oscillations $f_{\text{osc}} = 833.3(3)$ Hz is 10 times higher than the frequency of rotation $f_{\text{rot}} = 83.3(3)$ Hz. All other parameters are selected according to the operating conditions of the propeller discussed in Section 4, specifically an ambient pressure of $p_0 = 101325$ Pa and an ambient temperature of $T_0 = 290.2$ K.

The overall sound pressure level (OASPL) in decibels (dB) is assessed using the formulae below:

$$\text{(3.1)} \quad \text{OASPL, dB} = 10 \log \left(\frac{p'_{\text{rms}}}{p'_{\text{ref}}} \right)^2, \quad p'_{\text{rms}} = \sqrt{\frac{1}{N} \sum_{k=1}^{N} p'^2_k}, \quad p'_{\text{ref}} = 20\,\mu\text{Pa},$$

where p'_{rms} is the root mean square of acoustic pressure p', p'_{ref} is the threshold of human hearing, N is the signal sample count, and p'_k are the successive p' values. Furthermore, acoustic pressure p' waveforms are converted from the time into the frequency domain using the discrete fast Fourier transform (DFFT) and presented as the sound pressure level SPL (dB) spectra for the first 20 rotor harmonics.

3.3. Numerical solution of the elementary aeroacoustic problem

The analytical solution obtained for the moving/unsteady point source of momentum and expressed by Eq. (2.4) is discretized in emission time τ using Tecplot 360 EX macro command language directives and applied as a reference for this validation. Conversely, for numerical solution (FW–H solver) based on Farassat's formulation 1A in the form of integral Eq. (2.3), the elementary point source is replaced with a single rectangular acoustic panel of 1 mm × 1 mm dimensions and orientation depicted in Fig. 1 (red color). Both solutions advance using the same source time-step $\Delta\tau$ equivalent to 0.025° of azimuth and for a duration of 2.5 rotation periods T_{rot} (14400/1440 samples per rotation/oscillation

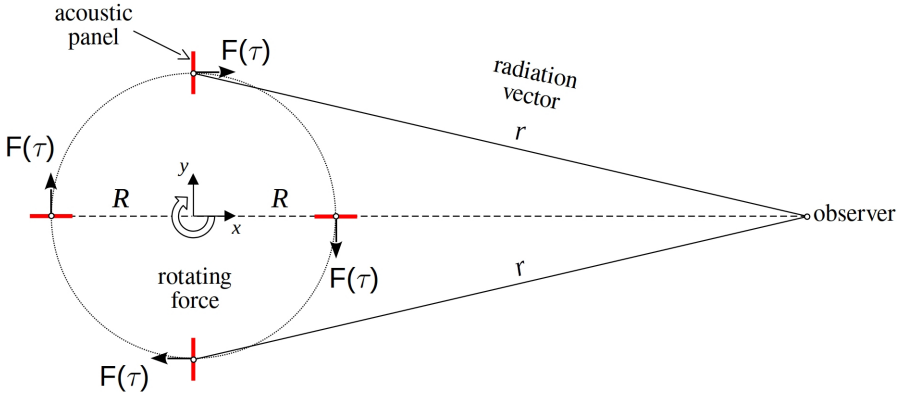

FIG. 1. Elementary moving point force.

period). Figure 2 presents the resultant acoustic pressure p' with the corresponding sound pressure level (SPL) spectra. Both the analytical and FW–H signals are equivalent, yielding an OASPL of 40.65 dB. Additionally, all depicted 20 rotor harmonics are accurately replicated with a precision of 0.003 Hz, validating the new functionality of the FW–H code. It is important to note that separate studies on the dependency of source time-step $\Delta\tau$ and acoustic panel dimensions have been conducted to confirm that the presented solutions remain unaffected by source/time discretization. Additionally, for verification purposes, different in-plane and out-of-plane force directions, as well as various observer positions regarding the rotor plane, were successfully validated; however, due to space constraints, this data is not included here.

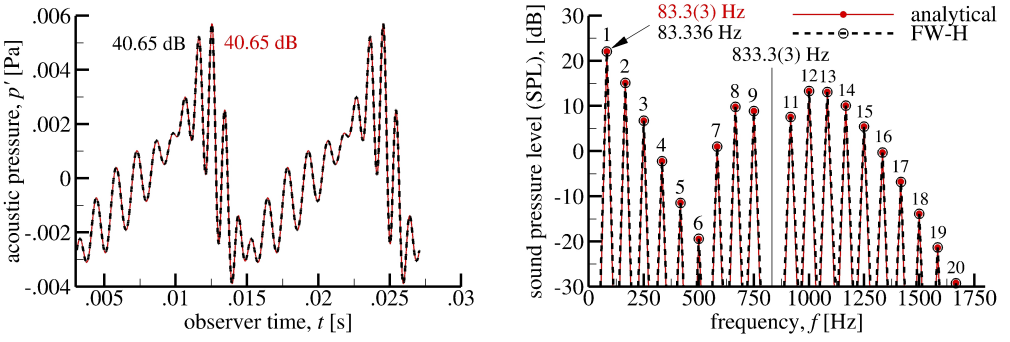

Fig. 2. Acoustic pressure p' signal in time (left) and frequency (right) domains.

4. Small-scale model UAV propeller (TUD)

4.1. Propeller design and wind tunnel test set-up

A small-scale model UAV propeller of the Delft University of Technology (TUD) is selected for analysis [8]. The rotor consists of two blades with a NACA 4412 airfoil section, a radius R of 0.15 m, and non-linear radial distributions for both the chord length c and the twist angle θ (see Fig. 3). The rotor's hub diameter is $D_{\mathrm{HUB}} = 0.027$ m, with an elliptical root section transitioning into the profiled section at a radius of 0.033 m ($c_{\mathrm{ROOT}} = 0.029$ m and $\theta_{\mathrm{ROOT}} = 43.7°$). The chord length reaches its maximum value of $c_{\mathrm{MAX}} = 0.034$ m and decreases towards the tip ($c_{\mathrm{TIP}} = 0.009$ m). The blades feature a total root-to-tip washout of $-31.4°$, resulting in a twist angle of $\theta_{\mathrm{TIP}} = 12.2°$ at the tip. The propeller is constructed from aluminum alloys, providing high stiffness and ensuring minimal elastic deformations during operation.

Experimental investigations of the propeller model were conducted by TUD in the semi-anechoic aeroacoustic open-jet wind tunnel (A-Tunnel) [8] – see

Fig. 3 (right). The model was positioned 0.5 m ahead of the exhaust of a convergent nozzle with a diameter of 0.6 m. The test chamber measured 3.2 m in height, with dimensions of 6.4 m by 4.4 m in length and width. For advance ratios $J = U_0/(f_{\mathrm{rot}}\, D)$ ranging from 0 to 0.8 and corresponding inflow velocities U_0 of up to 20 m/s, the mean streamwise velocity component remained uniform (with an accuracy of 0.6%), and turbulence intensity was maintained below 0.14%. For thrust and torque measurements, a load cell (maximum capacity of 22.2 N) and a torque sensor (maximum capacity of $0.18\,\mathrm{N}\cdot\mathrm{m}$) were utilized, both featuring non-linearity and hysteresis of ±0.1% of RO. Data was sampled at 5 kHz over a duration of 15 s and averaged in time. Furthermore, an optical encoder was employed to monitor the rotational speed (RPM) of the shaft. Noise measurements were conducted using 13 analog free-field microphones (with a frequency response of ±1 dB) arranged on a linear vertical microphone array positioned perpendicularly to the rotor plane. Microphone #7, adapted in the current investigation and marked in blue in Fig. 3, was located at the propeller plane, at a distance of $4D$ (1.2 m) from the propeller axis. For the data acquisition system, a sampling frequency of 51.2 kHz (sample length of 20 µs, equivalent to 0.6° of rotation) and a recording duration of 30 s were employed for each measurement. The chamber's cut-off frequency was roughly 200 Hz.

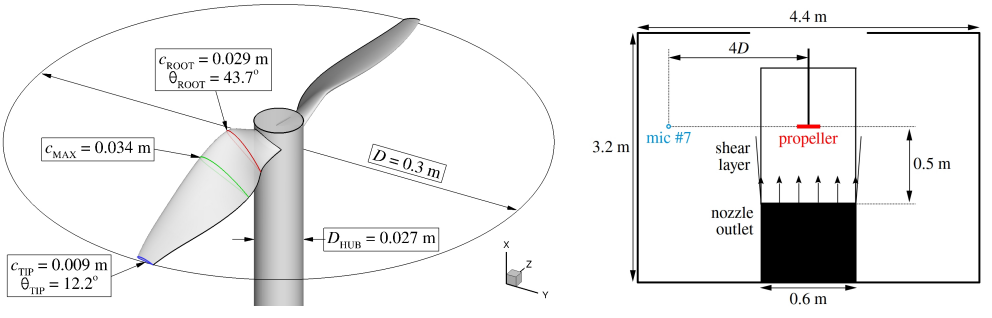

FIG. 3. Propeller design (left) and TUD A-Tunnel test set-up (right).

The propeller operated at a rotational speed of 5000 RPM (corresponding to a rotational frequency f_{rot} of 83.3(3) Hz), resulting in a tip Mach number M_{T} of 0.23 and a tip Reynolds number Re_{T} of $50 \cdot 10^3$. The advance ratios J ranged from 0 to 0.8 with an ambient pressure p_0 at 101325 Pa and a temperature T_0 at 290.2 K. The actual inflow Reynolds numbers varied between $50 \cdot 10^3$ and $100 \cdot 10^3$, based on the radial location and the advance ratio. Both natural and forced transition (tripping at 25% of the chord on the suction side) were examined experimentally; however, this study focuses solely on the tripped cases.

4.2. Block-structured FLOWer solver (DLR)

A block-structured compressible FLOWer solver (DLR) was employed to conduct the flow-field analysis of the propeller [14]. Steady simulations were performed using a standard second-order central scheme with artificial dissipation, coupled with the SALSA (strain adaptive linear Spalart–Allmaras [15]) 1-equation turbulence model (time integration by the explicit Runge–Kutta method). Unsteady simulations employed the delayed detached-eddy simulation (DDES) approach [16], utilizing the enhanced fourth-order accurate SLAU2 upwind scheme of Kitamura and Shima [17]. With the implementation of the Mach number scaling of numerical dissipation, this AUSM-type scheme maintains accuracy across incompressible, transonic, supersonic, and hypersonic flow regimes. A blend of second and third-order scheme BDF2OPT (optimized second-order backward difference scheme) was used for time integration [18]. For the "delayed" version of DES, the model stress depletion (MSD) issue (often leading to grid-induced separation) is avoided by appropriately selecting the shielding function within the boundary layers. In this hybrid RANS–LES method, the RANS branch (attached flow regions) utilizes the k–ω SST (shear-stress transport) 2-equation turbulence model [19] while in LES mode (areas of massive separation), this closure serves as a subgrid-scale model (rather than, for example, the Smagorinsky model) [20].

4.3. Computational set-up

The computational domain is cylindrical in shape, with the propeller positioned at its center (Fig. 4). The outer boundaries are located $10R$ above and $15R$ below the rotor plane, and $10R$ from the rotation axis. Two sets of struc-

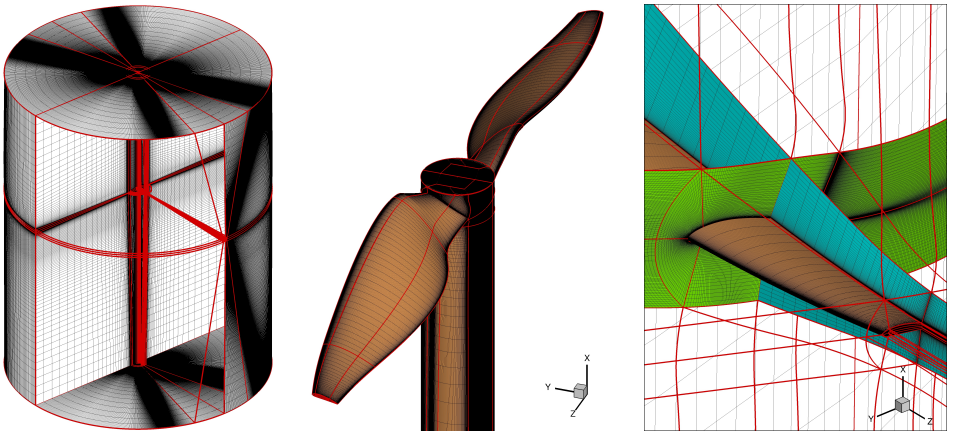

Fig. 4. Computational domain and grid topology (left), surface grid (middle), and tip-zoom (right) – RANS grid with 172 blocks and $95.6 \cdot 10^6$ of control volumes.

tured grids (2 blades, C-H-H topology, $y^+ < 1$) are prepared for either RANS or DES analysis. The RANS mesh consists of 172 blocks and $11.9 \cdot 10^6$ (medium) or $95.6 \cdot 10^6$ (fine) of control volumes. The refined DES grid (medium) contains 1496 blocks (parallel efficiency) and $20.5 \cdot 10^6$ of cells. The medium grids are constructed by removing every other mesh line from the respective fine grids. All meshes are generated semi-automatically using a developed series of Python scripts designed for the Interactive Grid Generator (IGG) application from the Fine/Turbo (Cadence) commercial software suite. The geometry of the propeller, the size of the domain, the mesh topology, and the number of cells in each direction for each block are parameterized, facilitating relatively simple adjustments to the existing grid. The RANS and DES meshes comprise 84% and 82% of good quality cells with orthogonality between 75° and 90°, respectively while only 4% of the total number of cells exhibit orthogonality below 60°, which is unavoidable in the tip region due to the sharp trailing edge of the rotor blade. The RANS grid refinement necessary for DES modeling facilitates an increase of the maximum aspect ratio from 14600 up to 65200 (low-impact control volumes located in the far-field). As the paper focuses on the development and validation of the computational framework, the entire workflow is demonstrated – from steady RANS (fully-turbulent, second-order) to unsteady RANS (transitional, high-order) and ultimately to DDES (transitional, high-order). This progression highlights how increasing model complexity improves the accuracy of sound emission and propagation predictions, thereby building confidence in the final results. Moreover, the standard RANS approach is crucial for evaluating the impact of grid resolution and determining the appropriate mesh refinement level for DDES simulations.

Flow simulations are conducted with a propeller in free-stream, using an inlet eddy viscosity ratio of 0.2 (the default value for SALSA closure) or 0.001 (the default value for k–ω SST closure). Additionally, the inlet turbulence intensity measured at 0.14% is applied for the two-equation model. Depending on the analyzed test flight characteristics (axial translation or hover), at the outer boundaries of the computational domain, either the characteristic variable far-field boundary condition ($J \neq 0$) or a specialized Froude boundary condition ($J = 0$) is imposed. The Froude boundary condition considers the induced velocities in the far-field resulting from the rotor's downwash in hover (source-sink model). Finally, solid surfaces are represented using the no-slip adiabatic wall boundary condition.

4.4. Aerodynamic analysis of the propeller

Figure 5 compares the total thrust coefficient c_t, rotor shaft torque coefficient c_q, and propulsive efficiency η_prop between the measurements from TUD and the FLOWer steady-state solutions (RANS/SALSA) in fully-turbulent mode

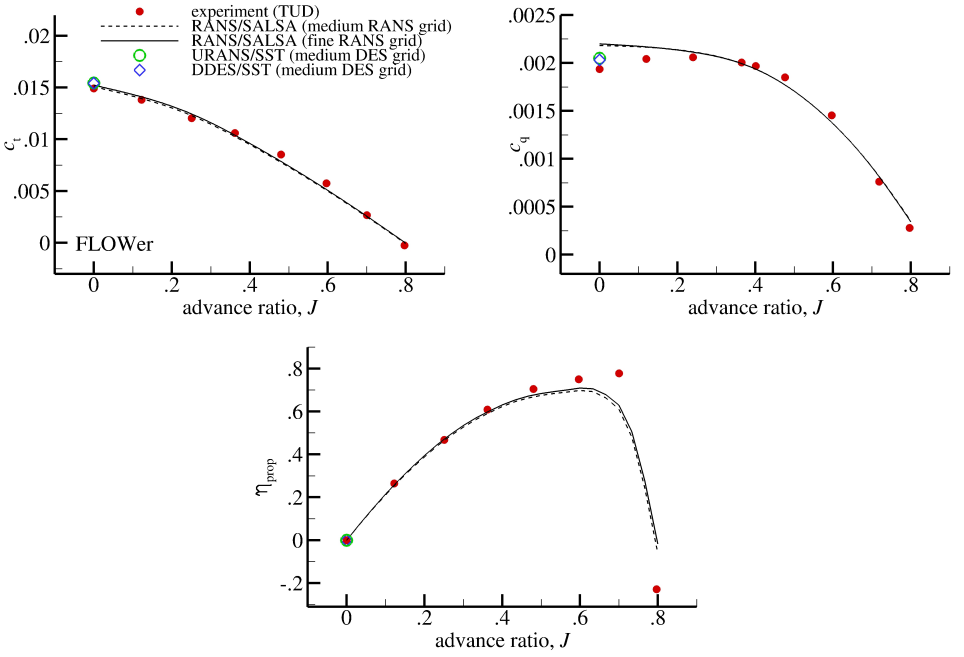

Fig. 5. Propeller thrust coefficient c_t (top left), torque coefficient c_q (top right), and propulsive efficiency η_prop (bottom).

for fine ($95.6 \cdot 10^6$ cells) and medium ($11.9 \cdot 10^6$ cells) RANS grids. The following formulae define the coefficients c_t, c_q, and η_prop:

$$c_\mathrm{t} = \frac{F_\mathrm{t}}{\rho_0 U_\mathrm{T}^2 \pi R^2}, \qquad c_\mathrm{q} = \frac{M_\mathrm{q}}{\rho_0 U_\mathrm{T}^2 \pi R^3}, \qquad \eta_\mathrm{prop} = \frac{c_\mathrm{t}}{c_\mathrm{q}} \frac{J}{\pi}, \tag{4.1}$$

where F_t and M_q represent the thrust force and torque, respectively (with a tip velocity $U_T = 78.5\,\mathrm{m/s}$ and an ambient density of $\rho_0 = 1.217\,\mathrm{kg/m^3}$) and η_prop signifies propulsive efficiency. The FLOWer solver operates in steady and fully-turbulent mode (using a classical second-order scheme), while the experimental data is collected with a boundary layer trip. Notable agreement of c_t is observed across the investigated range of J. A satisfactory correlation is also noticeable for c_q, primarily above $J = 0.2$. The slight overestimation of torque for $J < 0.2$ warrants further investigation (a similar effect is observed in the VLES simulations conducted at TUD and presented in [8]). The propulsive efficiency η_prop matches the test points until approximately $J = 0.6$, leading to a noticeable underestimation at $J = 0.7$ which might be attributed to small deviations in c_t and c_q, resulting from the numerical model deficiencies and relatively large absolute thrust and torque measurement uncertainties inherent for lower measured values. Lastly, the computations with medium and fine grids

yield virtually identical results for the total thrust and shaft torque, indicating mesh-independent solutions.

Given the limitations of unsteady RANS/SALSA modeling in capturing flow unsteadiness under the investigated hover conditions, the DDES approach using k–ω SST with transition tripping at 25% c (on the suction side only) was subsequently applied for $J = 0$ (DDES/SST). The FLOWer solver, utilizing the SLAU2 upwind scheme of fourth-order spatial accuracy and the BDF2OPT time integration scheme, along with a refined DES grid ($20.5 \cdot 10^6$ volumes) and a time-step of $\Delta t = 8.3 \cdot 10^{-6}$ s, equivalent to 0.25° of rotation (1440 time-steps per revolution), yields mean values for the rotor thrust c_t and shaft torque c_q coefficients that are comparable to previous RANS/SALSA predictions (see Fig. 5). Nevertheless, notable surface pressure fluctuations caused by separation can now be observed. Figure 6 presents an instantaneous distribution of the skin friction coefficient sign, with red color indicating areas of reversed flow, not only for DDES/SST but also for a reference solution denoted as "URANS/SST" (calculated also with the refined DES grid and high-order numerical scheme). Three distinct separation zones can be readily identified on the suction side. A large turbulent separation zone extends along the trailing edge across nearly the entire radial span of the blade. At the inboard stations, a second reversed flow region near the leading edge is evident, resulting from massive separation due to high local incidences. At the outer sections, significant flow detachment is observed, likely caused by both high inflow velocities and blade-vortex interaction – a collision between the leading edge and the tip vortex structure generated by the preceding blade. The latter two phenomena appear to be laminar, as the separation onset occurs upstream of the transition trip, particularly in the inboard regions.

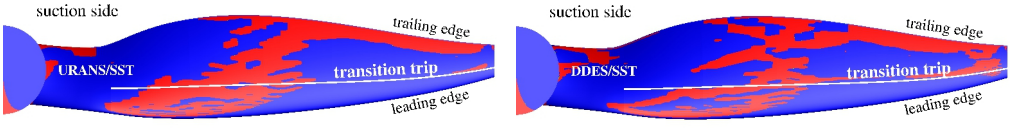

FIG. 6. Instantaneous suction side skin friction coefficient sign (reversed flow areas) at $J = 0$ for URANS/SST (left) and DDES/SST (right).

Surface pressure data was collected over 2.5 revolutions (3600 files), time-averaged (p'_{rms}), and converted to the logarithmic scale (OASPL). The resultant suction and pressure side fluctuations are presented in Fig. 7 for URANS/SST (left) and DDES/SST (right) approaches to turbulence modeling. For DDES/SST (top right), the highest pressure fluctuation intensity is observed on the suction side, near the blade tip (peaking at 155.1 dB) and in the region of massive inboard separation (maximum of 146.8 dB). Interestingly, the unsteadiness

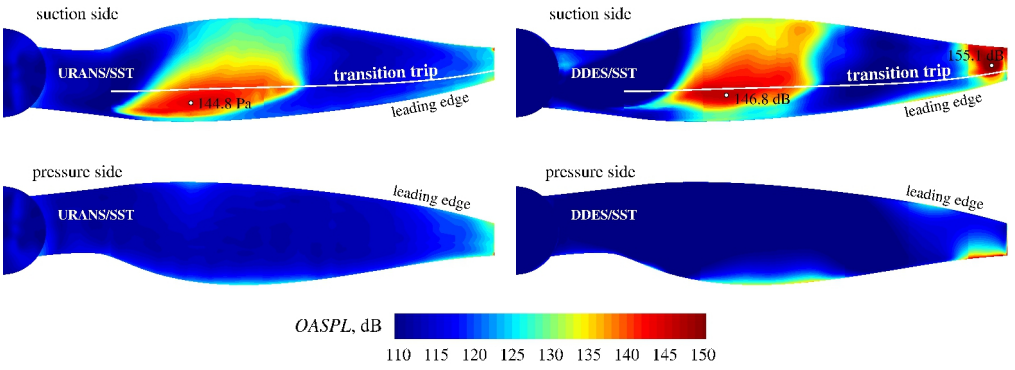

Fig. 7. Suction and pressure side surface pressure fluctuations (OASPL) at $J = 0$ for URANS/SST (left) and DDES/SST (right).

introduced by the trailing edge separation is not apparent at this scale. Conversely, on the pressure side (bottom right), there is a local rise in pressure fluctuations downstream of the two separated regions, attributed to the interaction between the flow structures and the trailing edge. Once again, a rise in pressure fluctuations is evident near the leading edge of the tip, reflecting the previously discussed blade-vortex interaction phenomenon. However, for URANS/SST modeling the depicted intensity of surface pressure fluctuations is notably reduced in magnitude and area coverage. Not only the inboard source is slightly attenuated (by 3 dB) but primarily the tip source is absent compared to the DDES/SST result. As a consequence, lowering the eddy viscosity based on the grid resolution and flow features (DDES), has a positive impact on the presence and strength of resolved acoustic perturbations.

4.5. Aeroacoustic analysis of the propeller

Three distinctive numerical sets of input surface pressure distributions, resulting from RANS/SST, URANS/SST, and DDES/SST modeling for $J = 0$ (hover), are provided for subsequent FW–H prediction of the acoustic signals at an in-plane microphone location positioned at a distance of 1.2 m, with numerical results shown in Fig. 8 (left). It is worth mentioning that all CFD solutions are progressed with the same refined DES grid ($20.5 \cdot 10^6$ of control volumes), time-step Δt of $8.3 \cdot 10^{-6}$ s (equivalent to 0.25° of rotation), fourth-order numerical scheme, and transition prescribed on the suction side of the blade at 25% c. Moreover, also the presented FW–H solutions are advanced with the same source-time step $\Delta\tau$ of 0.25° of azimuth, full-resolution surface mesh, and for 2.5 periods of rotation T_{rot} (the choices based on the performed acoustic grid, time-step, and duration time dependency studies).

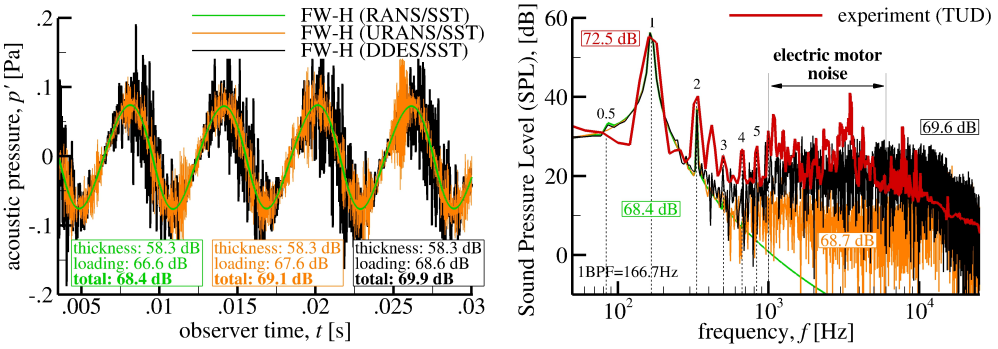

FIG. 8. Acoustic pressure p' (left) and sound pressure level (SPL) spectra (right) at $J = 0$.

The FW–H (RANS/SST) prediction is based on the averaged (mean) pressure distribution of the URANS/SST simulation, allowing for separation of the rotational noise from the broadband component. Therefore, the dominant mechanisms of acoustic radiation are attributed to thickness (mass displacement) and steady loading (mean aerodynamic forces) effects, leading to a quasi-sinusoidal acoustic pressure p' signal (green line in Fig. 8). In this case, the calculated overall sound pressure level (OASPL) based on Eq. (3.1) is equal to 68.4 dB, comprising the sum of the thickness (58.3 dB) and the dominating steady loading (66.6 dB) components. On the other hand, because URANS/SST flow results exhibit noticeable small-scale surface pressure fluctuations due to the presence of separation, the resultant acoustic signal depicted as "FW–H (URANS/SST)" (orange line) exhibits an unsteady loading component of broadband character, resulting in an increase of the total OASPL by 0.7 dB (up to 69.1 dB). Finally, the DDES/SST flow modeling results in significant unsteadiness of surface pressure distribution due to laminar and turbulent boundary layer separation and shear-layer instability. Therefore, the resultant acoustic signal, marked as "FW–H (DDES/SST)" (black line), represents an addition of the tonal noise with the effect of the rotating surface pressure fluctuations on account of flow detachment (broadband). Notably, this curve closely resembles the elementary solution shown in Fig. 2. In this case, the OASPL is slightly higher at 69.9 dB, resulting from the summation of the thickness (58.3 dB) and the loading (68.6 dB) components. It is important to note that the addition process depends not only on the amplitude but also on the phase of the component signals, leading to partial cancellation or augmentation effects.

For experimental validation of the presented results, the FW–H analysis is extended to 10 periods of rotation while increasing the time-step to $\Delta\tau = 1.67 \cdot 10^{-5}$ s (0.5° of azimuth), in line with the signal post-processing procedures at TUD (sampling frequency of 51.2 kHz, resulting in sample length equivalent to

0.6° of azimuth). Based on the initial acoustic grid dependency studies, two times coarser (in each direction) surface mesh (compared to the CFD grid) is sufficient to accurately resolve the propeller tonal and broadband source generation and propagation effects (introducing an uncertainty of less than 0.2 dB to OASPL). The final signals are transformed into the frequency domain using DFFT with rectangular windowing function and the resulting SPL spectra are compared with the wind tunnel test data from TUD, as shown in Fig. 8 (right). The FW–H (DDES/SST) solution captures both the harmonic (tonal) and broadband components of the propeller's acoustic signature, presenting a satisfactory correlation with the measurements (blade passing frequency of 166.7 Hz). The observed discrepancies can largely be attributed to experimental factors such as instantaneous variations in propeller RPM (±2 dB), electric motor noise in the 1 kHz to 6 kHz range, the presence of a shaft frequency peak (BPF = 0.5) and its harmonics due to blade imbalance, low-frequency background noise (< 200 Hz), and inflow unsteadiness caused by room recirculation during hover. However, the integration of the experimental and computational FW–H (DDES/SST) spectra (SPL) leads to a relatively small difference in OASPL of 2.9 dB (72.5 dB and 69.6 dB, respectively). On the contrary, the FW–H (URANS/SST) solution is characterized by a significantly reduced level of the broadband component (by 5 dB–20 dB), leading to an increased deviation from the measured OASPL of 3.8 dB (68.7 dB). Finally, the FW–H (RANS/SST) solution is purely tonal and lacks important broadband noise generation mechanisms (OASPL of 68.4 dB).

Because the propeller acoustic signature in terms of the unweighted overall sound pressure level is dominated by low-frequency (tonal) components, the A-weighting procedure is applied to the data to emphasize the difference in perception of the calculated signals (Fig. 9). A-weighting is a frequency-dependent curve (or filter) designed to adjust the SPL spectra to account for the nonlinear sensitivity of human hearing by minimizing the influence of low (<1 kHz)

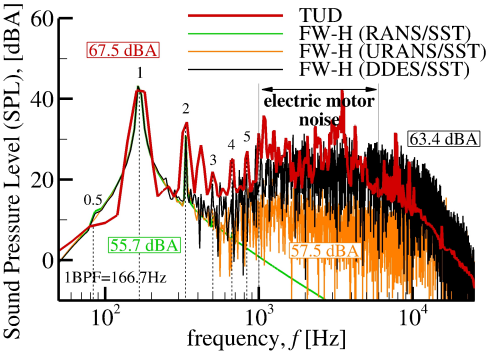

Fig. 9. A-weighted sound pressure level (SPL) spectra at $J = 0$.

and high (> 6 kHz) frequencies. For all depicted acoustic signals, i.e. FW–H (DDES/SST), FW–H (URANS/SST), and FW–H (RANS/SST), the thickness and steady loading components are practically equal, therefore the weighting procedure highlights solely the differences in resolved broadband noise generation (due to unsteady loading). The corresponding weighted OASPL values equal 63.4 dBA, 57.5 dBA, and 55.7 dBA, respectively. The deviation from the experimental value of 67.5 dBA increases from 4.1 dBA for FW–H (DDES/SST), through 10.0 dBA for FW–H (URANS/SST), up to 11.8 dBA for FW–H (RANS/SST) due to the decreasing intensity of resolved surface pressure fluctuations on account of flow phenomena. It is worth emphasizing that the 4.1 dBA difference is dictated mostly by the presence of electric motor noise (approx. 5 dBA–10 dBA) in the wind tunnel data, exactly in the 1 kHz to 6 kHz range of maximum audibility of human hearing.

5. Conclusions

This paper reports on the development and validation of a new computational framework designed for aeroacoustic predictions of noise radiation of small-scale propellers operating in the low-Reynolds number regime. The implemented algorithm relies on the FW–H analogy and is based on Farassat's formulation 1A of the solution to the FW–H equation, enabling tonal and broadband noise analysis. The validation process was initially performed for elementary rotating and oscillating momentum sources (forces) with available analytical solutions. Subsequently, the TUD propeller was simulated using the block-structured, compressible flow solver FLOWer which employs RANS/SALSA (fully-turbulent) and URANS/SST or DDES/SST (transitional) approaches, utilizing second- and fourth-order numerical schemes. The predicted rotor aerodynamic performance was compared to the experimental data (for tripped cases only) at a rotational speed of 5000 RPM (the tip Mach number of 0.23) across a wide range of advance ratios J. Finally, under challenging hover conditions and for an in-plane observer location (where maximum radiation occurs), the predicted surface pressure fluctuations were utilized as input for FW–H analysis, and the resulting propeller SPL signature was compared with the measured spectrum.

The newly developed computational framework includes Python software for semi-automatic propeller grid generation and setup, a set of Tecplot 360 EX macros for analyzing and preparing unsteady surface pressure distributions (mean pressure, p', and OASPL), an in-house FW–H solver modified to accept unsteady blade loading data, and post-processing Tecplot 360 EX macros for analyzing the resulting acoustic signals in both time (p') and frequency (SPL) domains. This simulation/analysis platform has proven capable of predicting propeller flow-field and acoustic emissions (both tonal and broadband) with

acceptable accuracy. Therefore, the proposed arrangement can be utilized in future studies on propeller noise reduction techniques. Nevertheless, the natural unsteadiness resulting from flow separation in the rotating system is highly sensitive to the computational grid and time-step resolutions, the specifics of the particular turbulence modeling approach, and the accuracy of the numerical scheme used, leaving some room for improvement. Additionally, cross-validation using another set of propeller experimental data could be advantageous, particularly in the absence of electric motor noise that contaminates the critical frequency range relevant to human perception. Lastly, the inclusion of the boundary layer transition prediction module of FLOWer is envisaged to extend the range of applicability of the tool.

Acknowledgments

This research was supported by the HPC center CI TASK in Gdansk (Poland).

References

1. S.A. Rizzi, D.L. Huff, D.D. Boyd, *Urban air mobility noise: current practice, gaps, and recommendations*, NASA Langley Technical Publication, TP-2020-5007433, 1–48, 2020.

2. D. Casalino, G. Romani, R. Zhang, H. Chen, *Lattice-Boltzmann calculations of rotor aeroacoustics in transitional boundary layer regime*, Aerospace Science and Technology, **130**, 107953, 1–12, 2022, https://doi.org/10.1016/j.ast.2022.107953.

3. A. Broatch, R. Navarro, J. García-Tíscar, F.N. Ramírez, *Evaluation of different FW-H surfaces and modal decomposition techniques for the acoustic analysis of UAV propellers through detached eddy simulations*, Aerospace Science and Technology, **146**, 108956, 1–12, 2024, https://doi.org/10.1016/j.ast.2024.108956.

4. O. Szulc, *Rotorcraft thickness noise control*, Archives of Mechanics, **73**, 4, 391–417, 2021, https://doi.org/10.24423/aom.3756.

5. P. Candeloro, D. Ragni, T. Pagliaroli, *Small-scale rotor aeroacoustics for drone propulsion: a review of noise sources and control strategies*, Fluids, **7**, 279, 1–23, 2022, https://doi.org/10.3390/fluids7080279.

6. E. Grande, D. Ragni, F. Avallone, D. Casalino, *Laminar separation bubble noise on a propeller operating at low Reynolds numbers*, AIAA Journal, **60**, 9, 5324–5335, 2022, https://doi.org/10.2514/1.J061691.

7. E. Grande, G. Romani, D. Ragni, F. Avallone, D. Casalino, *Aeroacoustic investigation of a propeller operating at low Reynolds numbers*, AIAA Journal, **60**, 2, 860–871, 2022, https://doi.org/10.2514/1.J060611.

8. D. Casalino, E. Grande, G. Romani, D. Ragni, F. Avallone, *Definition of a benchmark for low Reynolds number propeller aeroacoustics*, Aerospace Science and Technology, **113**, 106707, 1–16, 2021, https://doi.org/10.1016/j.ast.2021.106707.

9. E. GRANDE, S. SHUBHAM, F. AVALLONE, D. RAGNI, D. CASALINO, *Computational aeroacoustic study of co-rotating rotors in hover*, Aerospace Science and Technology, **153**, 109381, 1–12, 2024, https://doi.org/10.1016/j.ast.2024.109381.

10. J.E. FFOWCS WILLIAMS, D.L. HAWKINGS, *Sound generation by turbulence and surfaces in arbitrary motion*, Philosophical Transactions of the Royal Society of London, Series A, Mathematical and Physical Sciences, **264**, 1151, 321–342, 1969, https://doi.org/10.1098/rsta.1969.0031.

11. F. FARASSAT, *Derivation of formulations 1 and 1A of Farassat*, NASA Langley Technical Memorandum, TM-2007-214853, 1–20, 2007.

12. S.W. RIENSTRA, A. HIRSCHBERG, *An introduction to acoustics*, Technical University of Eindhoven Report, IWDE 01-03, 264–269, 2021.

13. T. SURESH, O. SZULC, P. FLASZYNSKI, *Aeroacoustic analysis based on FW–H analogy to predict low-frequency in-plane harmonic noise of a helicopter rotor in hover*, Archives of Mechanics, **74**, 2-3, 201–246, 2022, https://doi.org/10.24423/aom.3999.

14. J. RADDATZ, J.K. FASSBENDER, *MEGAFLOW-Numerical Flow Simulation for Aircraft Design; Chapter 2, Block structured Navier–Stokes solver FLOWer*, Notes on Numerical Fluid Mechanics and Multidisciplinary Design (NNFM), **89**, 27–44, 2005, https://doi.org/10.1007/3-540-32382-1.

15. T. RUNG, U. BUNGE, M. SCHATZ, F. THIELE, *Restatement of the Spalart–Allmaras eddy-viscosity model in strain-adaptive formulation*, AIAA Journal, **41**, 7, 1396–1399, 2003, https://doi.org/10.2514/2.2089.

16. P.R. SPALART, S. DECK, M.L. SHUR, K.D. SQUIRES, M.KH. STRELETS, A. TRAVIN, *A new version of detached-eddy simulation, resistant to ambiguous grid densities*, Theoretical and Computational Fluid Dynamics, **20**, 3, 181–195, 2006, https://doi.org/10.1007/s00162-006-0015-0.

17. K. KITAMURA, E. SHIMA, *Towards shock-stable and accurate hypersonic heating computations: a new pressure flux for AUSM-family schemes*, Journal of Computational Physics, **245**, 62–83, 2013, https://doi.org/10.1016/j.jcp.2013.02.046.

18. V.N. VATSA, M.H. CARPENTER, D.P. LOCKARD, *Re-evaluation of an optimized second order backward difference (BDF2OPT) scheme for unsteady flow applications*, Proceedings of the 48th AIAA Aerospace Sciences Meeting Including the New Horizons Forum and Aerospace Exposition, 4–7 January 2010, Orlando, USA, 2010-0122, 1–15, 2010, https://doi.org/10.2514/6.2010-122.

19. F.R. MENTER, *Two-equation eddy-viscosity turbulence models for engineering applications*, AIAA Journal, **32**, 8, 1598–1605, 1994, https://doi.org/10.2514/3.12149.

20. M.S. GRITSKEVICH, A.V. GARBARUK, J. SCHÜTZE, F.R. MENTER, *Development of DDES and IDDES formulations for the k-ω shear stress transport model*, Flow, Turbulence and Combustion, **88**, 431–449, 2012, https://doi.org/10.1007/s10494-011-9378-4.

Received October 21, 2024, revised version December 5, 2024.
Published online February 6, 2025.